Running title: An endocytic myosin-1 generates power

# Endocytic myosin-1 is a force-insensitive, power-generating motor

Ross TA Pedersen[1, 3, 4], Aaron Snoberger[2, 4], Serapion Pyrpassopoulos[2], Daniel Safer[2], David G Drubin[1*], E Michael Ostap[2*]

[1]Department of Molecular and Cell Biology, University of California, Berkeley, Berkeley, CA 94720

[2]Pennsylvania Muscle Institute, Perelman School of Medicine, University of Pennsylvania, Philadelphia, PA 19104

[3]Present address: Department of Embryology, Carnegie Institution for Science, Baltimore, MD 21218

[4]Equal Contribution

*Correspondence: drubin@berkeley.edu, ostap@mail.med.upenn.edu

15 **Summary**

16

17 Pedersen, Snoberger et al. measure the force-sensitivity of the yeast endocytic the myosin-
18 1 called Myo5 and find that it is more likely to generate power than to serve as a force-
19 sensitive anchor in cells. Implications for Myo5's role in clathrin-mediated endocytosis are
20 discussed.

21 **Abstract**

22 Myosins are required for clathrin-mediated endocytosis, but their precise molecular roles
23 in this process are not known. This is, in part, because the biophysical properties of the
24 relevant motors have not been investigated. Myosins have diverse mechanochemical
25 activities, ranging from powerful contractility against mechanical loads to force-sensitive
26 anchoring. To better understand the essential molecular contribution of myosin to
27 endocytosis, we studied the in vitro force-dependent kinetics of the *Saccharomyces*
28 *cerevisiae* endocytic type I myosin called Myo5, a motor whose role in clathrin-mediated
29 endocytosis has been meticulously studied in vivo. We report that Myo5 is a low-duty-ratio
30 motor that is activated ~10-fold by phosphorylation, and that its working stroke and actin-
31 detachment kinetics are relatively force-insensitive. Strikingly, the in vitro
32 mechanochemistry of Myo5 is more like that of cardiac myosin than like that of slow
33 anchoring myosin-1s found on endosomal membranes. We therefore propose that Myo5
34 generates power to augment actin assembly-based forces during endocytosis in cells.

35 **Introduction**

36

37 During clathrin-mediated endocytosis (CME), the plasma membrane invaginates and
38 undergoes scission to become a cytoplasmic vesicle. Coat proteins like clathrin can deform
39 membranes under low tension (Dannhauser and Ungewickell, 2012; Busch et al., 2015; Cail
40 et al., 2022), but when membrane bending is resisted by membrane tension (Hassinger et
41 al., 2017), the actin cytoskeleton drives plasma membrane invagination (Boulant et al.,
42 2011; Kaplan et al., 2022). In yeasts, including *Saccharomyces cerevisiae* and
43 *Schizosaccharomyces pombe*, turgor pressure opposes plasma membrane invagination, so
44 actin is required at every CME site (Aghamohammadzadeh and Ayscough, 2009; Basu et al.,
45 2013).

46 The actin cytoskeleton can produce pushing and pulling force, both of which are
47 required for CME in *S. cerevisiae* (Sun et al., 2006). When actin filament ends grow against a
48 surface, they push the surface forward (Mogilner and Oster, 1996, 2003). During CME, actin
49 filaments, bound by coat proteins, grow against the plasma membrane at the base the CME
50 site, driving invagination (Picco et al., 2015; Kaksonen et al., 2005, 2003; Skruzny et al., 2012,
51 Fig. 1). Modeling of the homologous CME machinery in mammalian cells has demonstrated
52 that such actin networks generate sufficient power for CME (Akamatsu et al., 2020), but
53 whether actin assembly alone can overcome turgor pressure in yeast cells is under debate
54 (Nickaeen et al., 2019; Carlsson, 2018).

55 Additional power may be provided by myosins, which generate tension on actin
56 filaments. The myosins critical for CME, Myo3 and Myo5 in budding yeast, and Myo1e in
57 vertebrates, are type I myosins (Geli and Riezman, 1996; Cheng et al., 2012; Krendel et al.,

58 2007). Some type I myosins are well-suited to generate power – i.e., they carry out
59 mechanical work per unit time by consuming ATP to execute a power stroke. Other type I
60 myosins are ideally suited to serve as force-sensitive anchors – their ATPase cycle is easily
61 arrested by resistance, locking them in a state that maintains tension without completing the
62 ATPase cycle or powering movement (Greenberg and Ostap, 2013). The possible roles of
63 type I myosins in CME depend on whether endocytic myosins are power generators or force-
64 sensitive anchors.

65 If endocytic type I myosins are acutely force-sensitive, they might organize the actin
66 filaments of the endocytic actin network, while if they are less force sensitive, they could
67 power plasma membrane invagination (Evangelista et al., 2000, Fig. 1). Myosin-1 motors
68 form a ring at the base of CME sites, where the invaginated membrane meets the plasma
69 membrane (Mund et al., 2018, Fig. 1). Yeast type I myosins serve at least one organizational
70 function as a membrane anchor for the actin assembly machinery, a function associated
71 with the non-motor tail of the molecules (Lewellyn et al., 2015), but motor activity is
72 required in addition to membrane anchorage (Pedersen and Drubin, 2019). If endocytic
73 myosin-1s are force sensitive anchors, they may serve a further organizational role by
74 holding growing filaments in an optimal orientation for force generation (Fig. 1, left). If the
75 myosins are power-generating motors, they may pull actin filament ends away from the
76 plasma membrane, deepening the plasma membrane invagination and creating space for
77 monomer addition and filament elongation (Fig. 1, right), a model supported by the
78 observation that the actin assembly rate at CME sites depends on type I myosin motors in a
79 dose-dependent manner (Manenschijn et al., 2019).

80 To distinguish between these possibilities, we measured the force sensitivity of the
81 endocytic myosin Myo5 (not to be confused with the vertebrate type V myosin). Myo5 is
82 insensitive to resistive force compared to related myosins. We therefore propose that Myo5
83 actively powers CME. Because actin and myosin collaborate in a variety of membrane
84 remodeling processes, we expect that these results will be instructive beyond CME.

## Results and Discussion

### Heavy Chain Phosphorylation Activates Myo5 ATPase Activity

To determine how force sensitive Myo5 is, we first needed to measure its unloaded kinetics. We purified a Myo5 construct containing the motor and lever domains from *S. cerevisiae* (Fig. 2A). Because phosphorylation of Myo5 at the TEDS site is required for most CME events and is thought to regulate Myo5's motor activity (Grosshans et al., 2006; Sun et al., 2006; Bement and Mooseker, 1995), we purified a phosphorylated version and an unphosphorylated version of the protein separately (See Materials and methods). p21 activated kinase was used to phosphorylate the myosin at the TEDS site (S357), as determined by control experiments with an S357A mutant (Fig. S1). The phosphorylation state of preparations was judged to be uniform when ATP-induced actoMyo5 dissociation transients were well fit by single exponential functions (see below). The yeast light chain for Myo5, calmodulin (Cmd1, Geli et al., 1998) was purified from *E. coli* and included in excess in all experiments (Fig. 2A).

We measured the steady-state actin-activated ATPase activities of phosphorylated and unphosphorylated Myo5 using the NADH-coupled assay (De La Cruz and Ostap, 2009) in the presence of 0 - 80 μM phalloidin-stabilized actin. Unphosphorylated Myo5 ATPase activity was largely insensitive to actin: the ATPase rate for at 0 μM actin was 0.14 $s^{-1}$, while the maximum ATPase rate measured was 0.39 $s^{-1}$ at 40 μM actin. (Fig. 2B). Phosphorylation activated Myo5 ATPase activity by about 10-fold (Fig. 2B). The actin concentration dependence of the phosphorylated Myo5 ATPase rate ($k_{\mathrm{obs}}$) was well fit by:

$$k_{obs} = v_o \frac{V_{\max}[Actin]}{K_{\mathrm{ATPase}}+[Actin]} \qquad \textbf{(Equation 1)}$$

108 From the fit, the actin concentration at half-maximum of the ATPase rate ($K_{\mathrm{ATPase}}$) was
109 determined to be 5.1 ± 0.88 μM, and the maximum ATPase rate ($V_{\mathrm{max}}$) was found to be 3.3 ±
110 0.15 $s^{-1}$ (Fig, 2B; Table 1).
111

112 **ATP Binding and ADP Release are Non-Rate Limiting for Myo5 ATPase Activity**

113 Resistive force impacts the rate of myosin detachment from actin, and two biochemical
114 transitions, ADP release and subsequent ATP binding, determine the detachment rate.
115 Therefore, we used stopped-flow kinetics to measure ADP release from (Fig. 2C, $k_{+5}$') and
116 ATP binding to (Fig. 2C, $K_1$' and $k_{+2}$') actoMyo5.
117 We found that yeast Myo5 does not quench the fluorescence of actin labeled at cys-374
118 with pyrene iodoacetamide, which is the probe most used to measure actomyosin
119 attachment and detachment (De La Cruz and Ostap, 2009). Thus, we measured actoMyo5
120 detachment by monitoring light scattering, which decreases as myosin unbinds actin.
121 To determine the rate constant for ATP binding, we mixed nucleotide-free actoMyo5
122 (100 nM) with varying concentrations of ATP and monitored 90° light scattering in the
123 stopped-flow instrument. Light scattering time courses followed single exponential
124 functions (Fig 2D). For phosphorylated Myo5, the observed rates determined from the fits
125 increased linearly with ATP concentration (Fig. 2E). At concentrations of > 1 mM ATP, the
126 actomyosin complex dissociated within the response time of the instrument, precluding
127 measurement. For unphosphorylated Myo5, the observed rates fit a rectangular hyperbola
128 with increasing ATP concentration (Fig. 2E).

The mechanism was modeled as (De La Cruz and Ostap, 2009):

$$AM + ATP \overset{K_1'}{\rightleftharpoons} AM(ATP) \overset{k_2'}{\longrightarrow} AM.ATP \overset{k_{diss}}{\longrightarrow} A + M.ATP\,, \quad \textbf{(Scheme 1)}$$

where $K_1$' is a rapid equilibrium binding step, $k_2$' is a rate-limiting isomerization to the AM.ATP state, and $k_{diss}$ is the rapid actin dissociation step. The apparent second order rate constant for ATP binding to phosphorylated actoMyo5 was determined by a linear fit to the data ($K_1'k_2'$ = 0.39 ± 0.017 μm$^{-1}$ s$^{-1}$). The unphosphorylated actoMyo5 data were fit by:

$$k_{obs} = \left[\frac{K_1'\,[ATP]}{1+K_1'\,[ATP]}\right] k_2'\,, \qquad \textbf{(Equation 2)}$$

and the maximum rate of isomerization ($k_2$' = 290 ± 24 s$^{-1}$) and ATP affinity ($K_1'$ = 0.006 ± 0.0016 μM$^{-1}$) were determined. The apparent second-order rate constant for ATP binding ($K_1'k_2'$) was determined from a linear fit of the observed rates below 100 μM ATP to be 1.1 ± 0.28 μM$^{-1}$ s$^{-1}$ (Table 1).

The rate constant for ADP dissociation ($k_{+5}$') was measured by preincubating 100 μM ADP with 200 nM actoMyo5 and then rapidly mixing with 2.5 mM ATP as shown in **scheme 2**:

$$A.M.ADP \overset{k_5'}{\rightleftharpoons} A.M + ATP \rightleftharpoons A.M(ATP) \longrightarrow A + M.ATP\,, \quad \textbf{(Scheme 2)}$$

When myosin active sites are saturated with ADP, the rate of ATP-induced dissociation of actomyosin is limited by ADP's slow dissociation. Light scattering transients were fitted by single exponential functions, yielding rates for ADP release for phosphorylated actoMyo5 ($k_{+5}$' = 74 ± 2.0s$^{-1}$) and for unphosphorylated actoMyo5 ($k_{+5}$' = 107 ± 5.9 s$^{-1}$) (Fig. 2F and Table 1). The signal-to-noise ratio of the fast light scattering transients is low, resulting in large uncertainties on these fits. However, these rates are substantially faster than the

152 steady-state ATPase values, but slower than the maximum rate of ATP-induced actomyosin
153 dissociation. ADP release for actoMyo5 ADP is much faster than ADP release for vertebrate
154 Myo1b and Myo1c (Greenberg et al., 2012; Lewis et al., 2006). It is more similar to the
155 vertebrate endocytic myosin-1, Myo1e (El Mezgueldi et al., 2002). Because ADP release is
156 rate limiting for detachment of Myo5 and Myo1e from actin, fast ADP release by these
157 molecules mean that the unloaded actin-attachment lifetimes for endocytic type I myosins
158 are < 15 ms. This property may make these motors particularly well-suited to function in
159 dynamic actin networks like those at CME sites, where actin filaments elongate and
160 "treadmill" into the cytoplasm (Kaksonen et al., 2003, 2005).
161

162 **Actin gliding is dependent on Myo5 phosphorylation state**

163 Our kinetic results suggest that both phosphorylated and unphosphorylated Myo5 have
164 low duty ratios (i.e., the motor spends a small fraction of its ATPase cycle bound to actin).
165 Since ADP release limits the rate of phosphorylated Myo5 detachment from actin at
166 saturating ATP ($k_{+5}$' = 74 ± 2.0 $s^{-1}$) and since we have measured the overall ATPase rate
167 ($V_{max}$ = 3.3 ± 0.15 $s^{-1}$), we can estimate the duty ratio:

168 $$Duty\ Ratio = \frac{(\frac{1}{k\prime_5})}{(\frac{1}{Vmax})}, \qquad \textbf{(Equation 3)}$$

169 The calculated duty ratio of phosphorylated Myo5 is 0.045. Unphosphorylated Myo5 has a
170 lower duty ratio (< 0.004).

171 To assess the effect of phosphorylation on Myo5 motility, we performed in vitro
172 motility assays at 1 mM ATP. Motors were attached site-specifically to coverslips coated
173 with anti-$His_6$ antibody. Coverslips were incubated with a range of concentrations of

174 phosphorylated and unphosphorylated Myo5, creating a titration series of surface
175 densities. At low Myo5 surface densities (incubation with ≤ 30 nM phosphorylated Myo5,
176 ≤ 150 nM unphosphorylated Myo5), actin filaments failed to bind the coverslip (Fig. 2G and
177 movies S1 and S2). At higher concentrations, phosphorylated Myo5 moved actin filaments
178 at velocities ranging from 720 ± 40 nm/s (100 nM phosphorylated Myo5) to 880 ± 90 nm/s
179 (40 nM) (Fig. 2G and movie S1). These gliding velocities are considerably higher than those
180 reported by Sun et al., 2006, possibly reflecting differences in the phosphorylation state of
181 the purified Myo5 protein (see below) or differences in other motility assay conditions,
182 such as light chain availability. Higher (> 5-fold) surface densities of unphosphorylated
183 Myo5 were required to achieve smooth motility, but this motility occurred at a
184 substantially slower speed, ~120 nm/s (Fig. 2G and movie S2). While it is possible that
185 residual phosphorylated Myo5 in the unphosphorylated prep contributed to this motility,
186 Sun et al., 2006 similarly reported that Myo5 harboring TEDS site mutations moved actin
187 filaments much more slowly. The slower actin gliding speed for unphosphorylated myosin
188 was unexpected given the similar rates of ADP release between phosphorylated and
189 unphosphorylated Myo5 (Table 1). It is possible that the our kinetics experiments have not
190 determined the rate limiting step for detachment, but it is more likely that motility of the
191 unphosphorylated myosin is limited by the slow attachment rate of the motor (Stewart et
192 al., 2021), as suggested by the slow actin-activated ATPase rate. The activation of Myo5
193 motility by phosphorylation could explain why fast, cargo-induced endocytosis, which
194 involves rapid and dynamic actin turnover, requires phosphorylated Myo5, while slower
195 constitutive endocytosis does not (Grosshans et al., 2006).
196

197 **Myo5's working stroke comprises two substeps that are consistent with unloaded**
198 **kinetic measurements**

199 The kinetics of actin attachment durations and mechanics of single myosin molecules were
200 measured using an optical trapping instrument that can detect sub-nanometer
201 displacements with millisecond temporal resolution (Woody et al., 2018; Snoberger et al.,
202 2021). We used the three-bead optical trapping geometry in which a biotinylated actin
203 filament is held between two laser-trapped polystyrene beads coated with neutravidin,
204 creating a bead-actin-bead dumbbell (Fig. 3A). Dumbbells were lowered onto pedestal
205 beads that were sparsely coated with phosphorylated Myo5-$His_9$ bound to a surface-
206 adsorbed anti-$His_6$ tag antibody. The positions of trapped beads were detected via
207 quadrant photodiode detectors, and single actomyosin binding events were detected by the
208 decrease in covariance of the positions of the two dumbbell beads (Fig. 3B-D).

209 Traces acquired at 1, 10, and 1000 μM ATP reveal displacements and drops in
210 covariance during actomyosin binding events. Individual points from covariance traces
211 were fit by double gaussian distributions, with the thresholds for event detection indicated
212 as dotted gray lines in Fig. 3 B-D. Event durations decreased with increasing ATP
213 concentrations (Fig. 3 B-D, blue lines).

214 The myosin-1 working stroke has been shown to occur in two discrete substeps,
215 with the first substep occurring with actin-activated phosphate release, and the second
216 occurring with ADP release (Jontes et al., 1995; Veigel et al., 1999, Fig. 3E). The substeps
217 can be characterized in optical trapping assays by ensemble averaging single interactions
218 (Veigel et al., 1999; Chen et al., 2012; Laakso et al., 2008), where the detected events are

219 aligned at their beginnings and forward-averaged in time (Fig 3F-H, left), or aligned at their
220 ends and reverse-averaged in time (Fig 3F-H, right).

221 Ensemble averages of Myo5 interactions showed a two-step working stroke at the
222 three ATP concentrations, but the step-size was most accurately resolved at 10 μM ATP
223 (see Materials and methods). In this condition, an initial substep of 4.8 nm was followed by
224 a second substep of 0.2 nm (Fig. 3G). We determined the lifetimes of the substeps by fitting
225 the ensemble averages with single exponential functions. At 1 μM ATP (Fig. 3F, left trace),
226 the measured rate (> 30 $s^{-1}$) of the time-forward average was limited by the covariance
227 smoothing window, but at 10 and 1000 μM ATP (Fig. 3 G-H, left traces), the rates were 49 ±
228 1.6 and 50 ± 0.2 $s^{-1}$, respectively (Fig. 3K) which are similar to the measured ADP release
229 rate ($k_{+5}$', 74 ± 2.0 $s^{-1}$, Table 1) supporting the model that the transition from state-1 to
230 state-2 accompanies ADP release.

231 The kinetics of time-reversed averages reveal the lifetime of State 2 (Fig. 3F-H, right
232 traces). Fitting single exponential functions to these traces reveals rates of 0.59 ± 0.003 and
233 7.34 ± 0.1 $s^{-1}$ at 1 and 10 μM ATP, respectively (Fig. 3K). At 1000 μM ATP, the observed rate
234 (> 187 $s^{-1}$) was limited by the size of the covariance smoothing window (5.25 ms; Fig. 3K).
235 The observed rates at 1 and 10 μM ATP are consistent with the second order rate constant
236 for ATP binding of 0.39 ± 0.017 $\mu M^{-1}s^{-1}$ measured by stopped-flow kinetics ($K_1$'$k_{+2}$',
237 Table 1).

238 We determined the detachment rates of actomyosin events by plotting the
239 cumulative frequency of individual attachment durations and fitting a single exponential
240 function to the data by maximum likelihood estimation (Fig. 3I). Data from 1 and 10 μM
241 ATP were well fit by single exponentials with rates of 0.88 and 6.87 $s^{-1}$, respectively (Fig. 3I,

242 Fig. 3K). These rates match well with the observed rate of ATP binding (Table 1), as well as
243 the fits for the reverse ensemble averages, indicating that at sub-saturating ATP (1 and 10
244 μM), detachment is limited by ATP binding (Figure 3J, blue squares & gray diamonds, Fig.
245 3K). Data from 1000 μM ATP were best described as the sum of 2 exponentials, with the
246 major rate of 67.8 $s^{-1}$ comprising 92.1% of the total, and a minor rate of 11.6 $s^{-1}$ comprising
247 7.9% of the total (Fig. 3I, Fig. 3K). The major rate is consistent with both the observed ADP
248 release rate and the measured forward ensemble average rates, indicating that at
249 saturating ATP, ADP release limits detachment of actomyosin interactions (Fig. 3J**,** blue
250 square and black diamond, Fig. 3K).
251

252 **Myo5 is a relatively force-insensitive motor**

253 To elucidate the force sensitivity of Myo5, we measured how its actin detachment rate was
254 affected by mechanical force opposing the power stroke using an isometric feedback
255 system that maintained the actin filament near its initial position (Takagi et al., 2006). The
256 initial force applied to Myo5 in this system depends in part on where along the actin
257 filament Myo5 stochastically binds, so this approach allowed measurement of attachment
258 durations at a range of resistive forces (Fig. 4A). Plotting attachment durations as a
259 function of force revealed a general trend of longer attachment durations at higher
260 resisting forces. At each interaction force, attachment durations are exponentially
261 distributed and, as expected based on prior isometric feedback experiments, the data
262 appear noisy when plotted this way (Fig. 4A). Converting these data to detachment rates by
263 binning them by force at every ten points, averaging, and taking the inverse of the
264 attachment duration more clearly reveals the trend (Fig. 4B).

265 The force dependence of the Myo5 detachment rate was fit by the Bell Equation:

266 $$k(F) = k_0 \cdot e^{\frac{-F \cdot d}{k_B \cdot T}}$$ (**Equation 4**)

267 where *k(F)* is the detachment rate at force *F*, $k_0$ is the detachment rate in the absence of
268 load, *d* is the distance parameter (the distance to the force-dependent transition state and a
269 measure of force sensitivity), $k_B$ is Boltzmann's constant, and *T* is the temperature. Best fit
270 parameters for $k_0$ and *d* were determined by maximum likelihood estimation of the
271 unaveraged data from Fig. 4A, incorporating the instrument response time (15-30 ms,
272 Woody et al., 2016). The estimated detachment rate in the absence of force is 67.6 $s^{-1}$, in
273 close agreement with the measured detachment rate under low load conditions at 1000 μM
274 (saturating) ATP (67.8 $s^{-1}$, Fig. 3K). The best fit value for the distance parameter, *d*, was
275 1.14 nm.

276 To put Myo5's force sensitivity in context, we re-plotted the function describing the
277 force-dependent actin detachment rate of Myo5 alongside the same curves for vertebrate
278 Myo1b, Myo1c, and β-cardiac myosin, which have previously been determined by the same
279 experimental approach (Fig. 4C, Laakso et al., 2010; Greenberg et al., 2012; Woody et al.,
280 2018). The mechanochemistry of Myo5 (*d* = 1.14 nm) is most like that of β-cardiac (muscle)
281 myosin (*d* = 1.3 nm), suggesting that it is well-suited for generating power. The difference
282 between Myo5 and acutely force-sensitive Myo1b, a tension-sensitive anchor myosin (*d* =
283 15 nm), is dramatic. From 0 to 2 pN of resistance, Myo1b attachment lifetimes slow from
284 ~600 ms to ~45 s, resulting in negligible power generation (Fig. 4D). Over the same
285 interval, Myo5 attachment lifetimes slow very modestly from ~15 ms to ~25 ms, allowing

286 it to generate considerable power (Fig. 4D). Thus, Myo5 is unlikely to act as a force-
287 sensitive anchor in cells and is more likely to power movements against a resisting load.
288

289 **Proposed function of type I myosin in clathrin-mediated endocytosis**

290 Myo5 is one of the best-studied myosin-1 proteins in vivo. Quantitative live cell imaging
291 and electron microscopy have revealed that it is recruited to CME sites simultaneously with
292 initiation of actin assembly, where it concentrates at the base of the site as membrane
293 invagination proceeds (Jonsdottir and Li, 2004; Idrissi et al., 2008). Although it has long
294 been appreciated that the presence (Geli and Riezman, 1996; Goodson et al., 1996) and
295 mechanochemical activity (Sun et al., 2006) of type-1 myosins are required for CME, the
296 mechanistic contribution of motor activity to the dynamic actin network was unknown.
297 When it was discovered that some type I myosins are acutely force sensitive (Laakso et al.,
298 2008), it became apparent that these motors could have mechanochemical activities that
299 range from force-dependent anchoring to power generation during CME. However,
300 distinguishing among these possibilities has been difficult in cells. Mutant Myo5 molecules
301 lacking the motor head or bearing mutations intended to lock the ATPase in low and high
302 actin affinity states each block CME, results that do not reveal the mechanochemical role of
303 Myo5 (Lewellyn et al., 2015; Idrissi et al., 2012). Perhaps the most informative finding in
304 cells has been the observation that varying the number of type I myosins at CME sites
305 results in differences in actin assembly rates (Manenschijn et al., 2019). However, because
306 resistive load remodels growing branched actin networks in complex ways (Bieling et al.,
307 2016), even this finding did not clearly differentiate between the possible roles for
308 endocytic myosin-1s.

309 Here we have shown that Myo5's motor generates power rather than forming force-
310 sensitive catch bonds. The overall ATPase rate of Myo5 is slow relative to other power-
311 generating myosins, but its power stroke and detachment from actin are fast, and they slow
312 only modestly under load (Fig. 4C). Myo5's relative force insensitivity means it generates
313 steady power against resistance (Fig. 4D). Because Myo3 and Myo5 can each support CME
314 in the absence of the other, we suspect that Myo3 is similarly force-insensitive. Given the
315 structural and functional homology between Myo5 and vertebrate Myo1e, together with
316 the close agreement of their unloaded kinetics (El Mezgueldi et al., 2002), we also predict
317 the Myo1e generates biologically relevant power.
318 Our finding that Myo5's kinetics are relatively force insensitive lead us to interpret
319 the previously described dose dependence of actin assembly on the number of myosin-1s
320 at endocytic sites to mean that this motor moves actin filaments at CME sites to power
321 plasma membrane invagination and create space for new monomers to assemble
322 (Manenschijn et al., 2019, Fig. 1, right). On the order of 300 myosin molecules (Myo3 and
323 Myo5 combined) are present at CME sites, mostly where the invaginating membrane meets
324 the plasma membrane (Mund et al., 2018; Idrissi et al., 2008; Sun et al., 2019; Picco et al.,
325 2015). A related myosin, Myo1c, also binds membranes and can generate and sustain sub-
326 piconewton forces parallel to the plane of the membrane, and greater forces when moving
327 actin filaments away from the membrane or when diffusion within the bilayer is impeded
328 (Pyrpassopoulos et al., 2016). Myo5's diffusion is likely to be impeded by the many proteins
329 at the base of CME sites, and it may move actin filaments at an angle to the membrane it is
330 bound to. Actin subunits "treadmill" towards the cytoplasm in endocytic actin networks at
331 ~50-100 nm/s (Kaksonen et al., 2005, 2003), so Myo5's motility rate of 700-900 nm/s (Fig.

332 2G), which we would expect resistance to slow only modestly, is fast enough to do work on
333 the actin network as it assembles. We therefore expect that the myosins power membrane
334 invagination and relive load to accelerate actin assembly during CME.

335 Type I myosins are involved in a variety of membrane reshaping events in cells,
336 where they often interact with growing branched actin networks (Sokac et al., 2006;
337 Almeida et al., 2011; Joensuu et al., 2014; Krendel et al., 2007; Cheng et al., 2012), but the
338 relative contributions of myosin motor activity and actin assembly have rarely been
339 resolved. Here, we demonstrated that a type I myosin critical for CME, a process well-
340 known to be driven by actin assembly, generates power. Implication of endocytic type I
341 myosin as a force-insensitive motor suggests that actin assembly and myosin power
342 generation can be coordinated to do coherent work in membrane remodeling processes.

343 **Materials and methods**

344

345 **Reagents, proteins, and buffers**

346 ATP concentrations were determined spectrophotometrically after each experiment by
347 absorbance at 259 nm, $\epsilon_{259} = 15{,}400\ M^{-1}cm^{-1}$. For all ATP solutions, one molar equivalent of
348 $MgCl_2$ was included to make MgATP. Rabbit skeletal muscle actin was prepared and gel
349 filtered (Spudich and Watt, 1971). Actin concentrations were determined
350 spectrophotometrically by absorbance at 290 nm, $\epsilon_{290} = 26{,}600\ M^{-1}cm^{-1}$. All actin was
351 stabilized with one molar equivalent of phalloidin (Sigma). Steady-state, transient, and
352 single molecule experiments were performed at 20°C in KMg25 buffer (60 mM MOPS pH 7,
353 25 mM KCl, 1 mM EGTA, 1 mM $MgCl_2$, 1 mM DTT). Apyrase VII was obtained from Sigma.
354 Purity and concentration of purified proteins were determined by comparing in-gel
355 Coomassie blue staining to staining of known amounts of bovine serum albumin (Pierce).

356

357 **Expression and Purification of Cmd1**

358 The *S. cerevisiae* calmodulin gene *CMD1* was cloned from genomic DNA into a bacterial
359 expression plasmid with a sequence encoding $His_6$-TEV situated at the 5' end to generate
360 pDD2743. pDD2743 was transformed into Rosetta *E. coli*, optimized for expression
361 (Novagen). A saturated overnight culture in LB (10 g/L Bacto tryptone, 5 g/L Bacto yeast
362 extract, 10 g/L NaCl) was used to inoculate a 1 L culture in LB to $OD_{600}$ = 0.1. Cells were
363 grown to $OD_{600}$ = 0.6-1, induced with 0.5 mM IPTG for 5 hours at 37°C, pelleted at 4,225 x g
364 for 20 minutes at 4°C in a Sorvall SLA-3000 (fixed angle) rotor, washed with cold 20 mM
365 HEPES pH 7.5, and repelleted at 2,250 x g for 10 minutes at 4°C in a Jouan CR3i (swinging

366 bucket) centrifuge. Cell pellets were flash frozen in 45 mL lysis buffer (20 mM HEPES pH
367 7.5, 1 M KCl, 20 mM Imidazole). Upon thawing, cells were lysed by sonication, 2 mg DNase I
368 (Roche) and triton X-100 to 1% were added, and the resulting lysate was incubated on ice
369 for 30 minutes, then spun at 92,000 x g for 25 minutes in a Beckman Type 70 Ti rotor. The
370 supernatant was loaded onto a 1 mL HisTrap HP column (GE healthcare) preequilibrated
371 with binding buffer (20 mM HEPES pH 7.5, 500 mM KCl, 20 mM imidazole). The column
372 was washed with 20 mL binding buffer, and Cmd1 was eluted using a 30 mL linear gradient
373 from 0-100% elution buffer (20 mM HEPES pH 7.5, 500 mM KCl, 500 mM imidazole).
374 Fractions containing Cmd1 were pooled, Cmd1 was cleaved from $His_6$ with TEV protease
375 and dialyzed overnight at 4°C into low salt buffer (10 mM Tris pH 7, 25 mM NaCl, 2 mM
376 $MgCl_2$, 5 mM DTT). Following dialysis, purified, cleaved Cmd1 was bound to a MonoQ
377 column and eluted using a 10 mL linear gradient from 0-70% high salt buffer (10 mM Tris
378 pH 7, 1 M NaCl, 2 mM $MgCl_2$, 5 mM DTT). Fractions containing Cmd1 were pooled, dialyzed
379 into KMg50 buffer (60 mM MOPS pH 7, 50 mM KCl, 1 mM $MgCl_2$, 1 mM EGTA, 1 mM DTT,
380 5% glycerol), and stored at -80°C.
381

382 **Expression and Purification of Myo5**

383 Myo5 was coexpressed with the myosin chaperone She4 in *S. cerevisiae.* The *MYO5* open
384 reading frame (ORF) from *S. cerevisiae* was cloned from genomic DNA and truncated at
385 $Gly^{763}$, generating a construct containing the motor domain and both Cmd1-binding IQ
386 motifs of the lever arm. The *SHE4* ORF was cloned in its entirety from *S. cerevisiae* genomic
387 DNA. Both ORFs were ligated into a 2μ expression plasmid with a partially defective *LEU2*
388 gene (*leu2d*) to ensure high copy number, creating plasmid pDD2744 (parent vector

389 described in Roy et al., 2011). The *MYO5* ORF was situated with a sequence encoding
390 AviTag-TEV-$His_9$ at the 3' end. Expression of the *MYO5* and *SHE4* ORFs was driven by a
391 bidirectional Gal 1/10 promotor.

392 pDD2744 was transformed into D1074 yeast (Roy et al., 2011). Saturated overnight
393 cultures in synthetic minimal medium (1.5 g/L Difacto yeast nitrogen base, 5 g/L
394 ammonium sulfate, supplemented with 2% glucose 20 µg/mL adenine, L-histadine, L-
395 methionine, and 30 µg/mL L-lysine) were used to inoculate 1.5 L cultures in the same
396 media with raffinose substituted for glucose to $OD_{600}$ = 0.1. After 18 hours of growth at
397 30°C, cultures were induced with 2% galactose, Bacto yeast extract was added to 10 g/L,
398 and Bacto peptone to 20 g/L. After 8 hours of expression, the cells were harvested at 4,225
399 x g for 20 minutes at 4°C in a Sorvall SLA-3000 rotor, washed with 25 mL cold Milli-Q
400 water, repelleted at 2,250 x g for 10 minutes at 4°C in a Jouan CR3i centrifuge, resuspended
401 in 0.2 volumes of cold Milli-Q water, and drop frozen into liquid nitrogen. Lysis was
402 achieved through cryomilling (10 cycles of 3 minutes grinding with one minute cooldown)
403 in the large vials of a 6870 freezer/mill (SPEX Sample Prep).

404 Cell powders were thawed in binding buffer (10 mM Tris pH 7, 500 mM NaCl, 4 mM
405 $MgCl_2$, 2 mM ATP, 20 mM imidazole, 5 mM DTT) supplemented with 1 mM PMSF, 1 x
406 cOmplete protease inhibitor cocktail without EDTA (Roche), and 1 µM Cmd1. For
407 purification of phosphorylated Myo5, 1 µg Pak1 (Sigma, Brzeska et al., 1997, Fig. S1) was
408 included in the lysis buffer and 10 mM β-glycerophosphate, 5 mM sodium pyrophosphate,
409 and 50 mM sodium fluoride were included in all purification buffers. For purification of
410 unphosphorylated Myo5, 4000 units lambda phosphatase (NEB) and 1 mM $MnCl_2$ were
411 included in the lysis buffer. The lysate was then spun at 345,000 x g for 10 minutes at 4°C

412 in a Beckman TLA100.3 rotor, filtered through a 0.22 μm filter, and loaded onto a 1 mL
413 HisTrap HP column. The column was washed with wash buffer (Binding buffer with only
414 200 mM NaCl), and Myo5 was eluted using a 20 mL linear gradient from 0-100% elution
415 buffer (wash buffer with 1 M imidazole).

416 Fractions containing Myo5 were pooled and supplemented with Cmd1 to 1 μM. For
417 unphosphorylated Myo5 purification, a further 20,000 units lambda phosphatase were
418 added along with $MnCl_2$ to 1 mM and the fractions were incubated at 30°C for 30 minutes.
419 Purified protein was dialyzed through a 3.5 KDa MWCO membrane into 1 L storage buffer
420 (KMg50 with 50% glycerol) overnight at 4°C and again into 500 mL of the same buffer for 2
421 hours at 4°C, then stored at -20°C.

422

423 **Kinetic measurements**

424 Steady-state actin-activated ATPase activity was measured using the NADH enzyme-linked
425 assay in an Applied Photophysics (Surrey, UK) SX.18 MV stopped-flow apparatus (De La
426 Cruz and Ostap, 2009). One reaction syringe contained the ATP mix (200 μM NADH, 20
427 U/mL lactic dehydrogenase, 100 U/mL pyruvate kinase, 500 μM phopho(enol)pyruvate, 2
428 mM $MgCl_2$, 2 mM ATP in KMg25) and the other syringe contained the mixture of actin (0-80
429 μM) and myosin (100 nM) in KMg25. Concentrations above are post-mixing. After mixing,
430 the concentration of NADH loss due to ATP hydrolysis was monitored by absorbance at 340
431 nm ($\epsilon_{340}$ = 6,220 $M^{-1}cm^{-1}$), and the linear regions of the curve were fitted to a straight line
432 to determine ATPase activity.

433 ATP-induced dissociation of actoMyo5 was measured and analyzed as described (De
434 La Cruz and Ostap, 2009). Briefly, one reaction syringe contained ATP (0 – 2.7 mM) in

435 KMg25 and the other syringe contained 100nM Myo5 and 100 nM phalloidin-stabilized
436 actin. Reactants were rapidly mixed by the instrument, and light scattering at 90° was
437 acquired using a 450 nm excitation light and a 400 nm emission filter. Experimental
438 transients were fit by single exponentials using the software provided with the stopped-
439 flow apparatus. 1-7 traces were averaged together to generate each data point. 0.04
440 units/mL apyrase was added to solutions of actoMyo5 before mixing to remove
441 contaminating ADP and ATP. Unphosphorylated actoMyo5 required prolonged treatment
442 with apyrase to achieve sufficient signal, presumably because a larger fraction of the
443 population was bound to ATP left over from purification and because the actin-activated
444 ATPase rate of unphosphorylated Myo5 is slow. ADP release transients were acquired and
445 analyzed as above by preincubating 100 μM ADP with 200 nM actoMyo5 and then rapidly
446 mixing with 2.5 mM ATP. Concentrations reported are post-mixing.
447

448 **Motility assays**

449 Motility assays were carried out essentially as in (Lin et al., 2005). Double-sided Scotch
450 tape and vacuum grease were used to create flow chambers from a clean glass coverslip
451 (22 mm x 40 mm, #1.5, Fisher) and a glass coverslip coated with 20 μL nitrocellulose
452 (Ernest F. Fullam, Inc., catalog number 11180). A mouse monoclonal antibody against $His_6$
453 (Sigma), made 0.2 mg/mL in motility buffer (10 mM MOPS pH 7, 25 mM KCl, 1 mM EGTA, 1
454 mM $MgCl_2$, 1 mM DTT), was first added to the flow chamber, and incubated there for 5
455 minutes to coat the nitrocellulose-coated coverslip with the antibody. The flow chamber
456 was then blocked for 2 minutes with 2 mg/mL casein. Blocking coverslips with bovine
457 serum albumin (BSA) led to inferior gliding. Phosphorylated or unphosphorylated Myo5 in

458 motility buffer with 2 mg/mL casein, diluted to a range of concentrations as indicated in
459 Fig. 2G, was added to the flow chamber and incubated for 2 minutes, then the chamber was
460 washed once with motility buffer containing 1 mM ATP and 5 μM Cmd1 and three more
461 times with the same buffer without ATP. Motility was initiated by loading the chambers
462 with 5 nM rhodamine phalloidin-labeled actin filaments in motility buffer with 1 μM ATP, 5
463 μM Cmd1, 2 mg/mL casein, 0.4 mg/mL glucose oxidase, 0.08 mg/mL catalase, 5 mg/mL
464 glucose. Movies of actin motility in the flow chambers were recorded at room temperature
465 (~20˚C) on a Leica DMI3000 B microscope outfitted with a 100x, 1.4 NA plan apo objective
466 and a Retiga R6 CCD camera (Teledyne), controlled by Metamorph software. The rate of
467 actin filament gliding was determined using the manual tracking plugin in Fiji.
468

469 **Optical trapping**

470 Flow chambers for optical trapping were constructed with double-sided tape and vacuum
471 grease as previously described (Snoberger et al., 2021; Greenberg et al., 2017). Briefly, the
472 coverslip was coated with a 0.1% mixture of nitrocellulose and 2.47 μm diameter silica
473 beads. Coverslips were dried at least 30 minutes and were used within 24 hours of
474 preparation. To define the walls of the flow cell, 2 strips of double-sided tape were placed
475 ~5 mm apart, a 1 mm thick glass slide was placed on top, and carefully sealed with vacuum
476 grease after addition of final buffer.
477 Trapping buffer (KMg25 with 1 mM DTT freshly added) was used for all trapping
478 assays. A 100x stock of glucose oxidase + catalase (GOC) was freshly prepared by
479 centrifuging catalase (Sigma, > 30000 $U \cdot mL^{-1}$) at 15,000 x g for 1 minute, and adding 2 μl of
480 catalase supernatant to 20 μL of 19.1 U/μL glucose oxidase (Sigma).

481 0.01 mg/mL anti-$His_6$ antibody (Sigma) was flowed in the chamber and incubated
482 between 30 seconds and 3 minutes, then immediately blocked with two, 3-minute
483 incubations of 1 - 2 mg/mL BSA. Stocks of phosphorylated $His_9$-tagged Myo5 were diluted
484 to 1 nM in trapping buffer with 300 mM added KCl and incubated in the flow cell for 2
485 minutes. The number of myosins bound to the surface was limited by the surface
486 concentration of anti-$His_6$ antibody, and the incubation time of anti-$His_6$ antibody was
487 adjusted daily between 30 seconds and 3 minutes such that 1 of 3 - 5 pedestals tested
488 showed clear myosin interactions with the actin dumbbell.
489 Following incubation with Myo5, a second blocking step with two, 3-minute
490 incubations of 1 - 2 mg/mL BSA was performed. Final buffer added to the flow cell
491 contained trapping buffer with indicated amount of ATP, 1 μL of GOC added immediately
492 prior to addition to chamber, and 0.1 - 0.25 nM rabbit skeletal muscle actin polymerized
493 with 15% biotinylated actin (Cytoskeleton) stabilized by rhodamine-phalloidin (Sigma) at a
494 1.1-1.2 molar ratio with G-actin concentration. Neutravidin-coated beads were prepared by
495 incubating 0.4 ng of 0.8 μm diameter polystyrene beads (Polysciences) and coated with 5
496 mg/mL neutravidin (Thermo Fisher). 3 μL of neutravidin-coated beads were added to one
497 side of the chamber prior to sealing. All trapping data were acquired within 90 minutes of
498 addition of the final buffer to the chamber.
499 Optical trapping experiments were performed at room temperature (20 ± 1 °C)
500 using a dual beam 1064 nm trapping laser as described in (Woody et al., 2018, 2017). A
501 single laser beam was split into 2 beams using polarizing beam splitters and steered into a
502 60x water immersion objective (Nikon). Laser light was projected through an oil
503 immersion condenser and into quadrant photodiodes (JQ-50P, Electro Optical Components,

504 Inc.), each of which were conjugate to the back focal plane of the objective. Direct force
505 detection from the quadrant photodiodes was achieved using a custom-built high-voltage
506 reverse bias and an amplifier. Data acquisition, beam position control output, and isometric
507 feedback calculations were controlled with custom-built virtual instruments (Labview,
508 Matlab).

509 Individual 0.8 μm diameter neutravidin-coated bead were caught in the two traps
510 and held approximately 5 μm apart. Trap stiffnesses were adjusted to 0.05 – 0.1 pN/nm for
511 each trap. A biotinylated actin filament visualized by rhodamine phalloidin was bound to
512 the two trapped beads, creating a bead-actin-bead dumbbell. The dumbbell was
513 pretensioned (3-5 pN) by steering one beam using a piezo controlled mirror conjugate to
514 the back focal plane of the objective, and the surface of pedestal beads were probed for
515 myosins. Putative myosin interactions were detected via drops in variance of the two
516 beads, and the 3-dimensional position of the dumbbell relative to the myosin was refined
517 further by maximizing the rate and size of the observed power stroke deflections. Every 30-
518 60 s, the dumbbell was moved axially along the actin filament in ~6 nm steps between
519 trace acquisition to ensure even accessibility of actin-attachment target zones. Stage drift
520 was corrected via a feedback system using a nano-positioning stage and imaging the
521 position of the pedestal bead with nm precision (Woody et al., 2017). In experiments using
522 1 μM ATP, due to the longer actomyosin interactions, stage drift was still observed even
523 with the stage feedback engaged, leading to a presumed underestimation of the
524 displacement size. All data were acquired at a sampling rate of 250 kHz.

525 Isometric optical clamping experiments were performed as described in (Woody et
526 al., 2018; Takagi et al., 2006) using a digital feedback loop and a 1-D electro-optical

527 deflector (EOD, LTA4-Crystal, Conoptics) to steer the beam position using input from a high
528 voltage source (Conoptics, Model 420 Amplifier). Briefly, the position of one bead (the
529 "transducer" bead) was maintained at a constant position by adjusting the position of the
530 other bead (referred to as the "motor" bead) during actomyosin interactions. The response
531 time of the feedback loop during actomyosin interactions was ~15-30 ms.
532

533 **Optical trap data analysis**

534 Actomyosin interactions for non-isometric optical clamping experiments were detected
535 using the single-molecule computational tool SPASM (Software for Precise Analysis of
536 Single Molecules , Blackwell et al., 2021), which uses a calculation of the dumbbell bead
537 covariances and a change-point algorithm. Data collected at 1000 μM ATP were analyzed at
538 250 kHz, while data collected at 1 and 10 μM ATP were downsampled to 2 kHz by
539 averaging every 125 points to enhance analysis speed. Events were detected by calculating
540 the covariance of the 2 beads using a smoothing window of 33.3, 15, and 5.25 ms and an
541 averaging window 60, 36, and 12 ms at 1, 10, and 1000 μM ATP, respectively. The
542 instrument deadtime was calculated to be 2 times the covariance averaging window. For
543 each 15 s trace, the detected covariance was plotted and fit to double gaussian
544 distributions, with the smaller mean gaussian corresponding to the actomyosin "bound"
545 portion and the larger mean gaussian corresponding to the "unbound" portion of events. A
546 putative event was defined as an event where the covariance starts above the unbound
547 peak mean, drops below the bound peak mean, and remains below the unbound peak mean
548 for at least the length of the instrument deadtime prior to returning back above unbound
549 peak mean. Event starts and ends were further refined using a changepoint algorithm as

550 described (Blackwell et al., 2021). Attachment durations and ensemble averages of single
551 events were determined using built-in features in the SPASM software. Exponential fits for
552 forward and reverse ensemble averages were performed in Origin 2019 graphing &
553 analysis software (OriginLab).
554 Events detected in isometric optical clamping experiments were detected as
555 described in (Takagi et al., 2006) using a zero crossing analysis via custom MATLAB scripts.
556 Briefly, when a myosin is actively engaged with the dumbbell, force is applied to the
557 transducer bead, a feedback loop is engaged and opposing force applied to the motor bead
558 until the position of the transducer bead is restored. Beginnings of events are defined at the
559 point at which the feedback signal increases from baseline in the motor bead, and ends of
560 events are defined when the feedback signal decreases back below the baseline in the
561 motor bead.
562
563 **Online supplemental material**
564 Figure S1 shows the results of a kinase assay demonstrating that Pak1, used to in
565 purifications of phosphorylated Myo5, specifically phosphorylates Myo5 serine-357.

## Acknowledgements

We thank M. Greenberg, E. Lewellyn, and A. Kunibe, each of whom played important roles at the inception of this study. We thank Y.E. Goldman for optical trap instrumentation. We thank M. Ferrin for helpful comments on the manuscript. This work was funded by National Institute of General Medical Sciences (NIGMS) grant R35 GM118149 to D.G.D and grant 5R37GM057247 to E.M.O. R.T.A.P. is currently funded by NIGMS F32 GM142145.

573 **References**

574

575 Aghamohammadzadeh, S., and K.R. Ayscough. 2009. Differential requirements for actin
576 during yeast and mammalian endocytosis. *Nat. Cell Biol.* 11:1039–1042.
577 doi:10.1038/ncb1918.
578 Akamatsu, M., R. Vasan, D. Serwas, M. Ferrin, P. Rangamani, and D.G. Drubin. 2020.
579 Principles of self-organization and load adaptation by the actin cytoskeleton during
580 clathrin-mediated endocytosis. *Elife*. 9:1–40. doi:10.7554/eLife.49840.
581 Almeida, C.G., A. Yamada, D. Tenza, D. Louvard, G. Raposo, and E. Coudrier. 2011. Myosin 1b
582 promotes the formation of post-Golgi carriers by regulating actin assembly and
583 membrane remodelling at the trans-Golgi network. *Nat. Cell Biol.* 13:779–789.
584 doi:10.1038/ncb2262.
585 Basu, R., E.L. Munteanu, and F. Chang. 2013. Role of turgor pressure in endocytosis in
586 fission yeast. *Mol. Biol. Cell*. 25:679–87. doi:10.1091/mbc.E13-10-0618.
587 Bement, W.M., and M.S. Mooseker. 1995. TEDS rule: A molecular rationale for differential
588 regulation of myosins by phosphorylation of the heavy chain head. *Cell Motil.*
589 *Cytoskeleton*. 31:87–92. doi:10.1002/cm.970310202.
590 Bieling, P., T. Li, J. Weichsel, R. Mcgorty, P. Jreij, B. Huang, D.A. Fletcher, and R.D. Mullins.
591 2016. Force Feedback Controls Motor Activity and Mechanical Properties of Self-
592 Assembling Branched Actin Networks. *Cell*. 164:115–127.
593 doi:10.1016/j.cell.2015.11.057.
594 Blackwell, T., W.T. Stump, S.R. Clippinger, and M.J. Greenberg. 2021. Computational Tool for
595 Ensemble Averaging of Single-Molecule Data. *Biophys. J.* 120:10–20.

596 doi:10.1016/j.bpj.2020.10.047.
597 Boulant, S., C. Kural, J.-C. Zeeh, F. Ubelmann, and T. Kirchhausen. 2011. Actin dynamics
598 counteract membrane tension during clathrin-mediated endocytosis. *Nat. Cell Biol.*
599 13:1124–31. doi:10.1038/ncb2307.
600 Brzeska, H., U.G. Knaus, Z.Y. Wang, G.M. Bokoch, and E.D. Korn. 1997. p21-activated kinase
601 has substrate specificity similar to Acanthamoeba myosin I heavy chain kinase and
602 activates Acanthamoeba myosin I. *Proc. Natl. Acad. Sci. U. S. A.* 94:1092–1095.
603 Busch, D.J., J.R. Houser, C.C. Hayden, M.B. Sherman, E.M. Lafer, and J.C. Stachowiak. 2015.
604 Intrinsically disordered proteins drive membrane curvature. *Nat. Commun.* 6.
605 doi:10.1038/ncomms8875.
606 Cail, R.C., C.R. Shirazinejad, and D.G. Drubin. 2022. Induced nanoscale membrane curvature
607 bypasses the essential endocytic function of clathrin. *J. Cell Biol.* 221.
608 doi:10.1083/jcb.202109013.
609 Carlsson, A.E. 2018. Membrane bending by actin polymerization. *Curr. Opin. Cell Biol.* 50:1–
610 7. doi:10.1016/j.ceb.2017.11.007.
611 Chen, C., M.J. Greenberg, J.M. Laakso, E.M. Ostap, Y.E. Goldman, and H. Shuman. 2012.
612 Kinetic schemes for post-synchronized single molecule dynamics. *Biophys. J.* 102.
613 doi:10.1016/j.bpj.2012.01.054.
614 Cheng, J., A. Grassart, and D.G. Drubin. 2012. Myosin 1E coordinates actin assembly and
615 cargo trafficking during clathrin-mediated endocytosis. *Mol. Biol. Cell*. 23:2891–904.
616 doi:10.1091/mbc.E11-04-0383.
617 Dannhauser, P.N., and E.J. Ungewickell. 2012. Reconstitution of clathrin-coated bud and
618 vesicle formation with minimal components. *Nat. Cell Biol.* 14:634–639.

619 doi:10.1038/ncb2478.
620 Evangelista, M., B.M. Klebl, A.H. Yong, B.A. Webb, T. Leeuw, E. Leberer, M. Whiteway, D.Y.
621 Thomas, and C. Boone. 2000. A Role for Myosin-I in Actin Assembly through
622 Interactions with Vrp1p, Bee1p, and the Arp2/3 Complex. *J. Cell Biol.* 148:353–362.
623 doi:10.1083/jcb.148.2.353.
624 Geli, M.I., and H. Riezman. 1996. Role of Type I Myosins in Receptor-Mediated Endocytosis
625 in Yeast. *Science*. 272:533–535.
626 Geli, M.I., A. Wesp, and H. Riezman. 1998. Distinct functions of calmodulin are required for
627 the uptake step of receptor-mediated endocytosis in yeast: The type I myosin Myo5p is
628 one of the calmodulin targets. *EMBO J.* 17:635–647. doi:10.1093/emboj/17.3.635.
629 Goodson, H. V, B.L. Anderson, H.M. Warrick, L.A. Pon, and J.A. Spudich. 1996. Synthetic
630 lethality screen identifies a novel yeast myosin I gene (MYO5): myosin I proteins are
631 required for polarization of the actin cytoskeleton. *J. Cell Biol.* 133:1277–1291.
632 doi:10.1083/JCB.133.6.1277.
633 Greenberg, M.J., T. Lin, Y.E. Goldman, H. Shuman, and E.M. Ostap. 2012. Myosin IC generates
634 power over a range of loads via a new tension-sensing mechanism. *Proc. Natl. Acad.*
635 *Sci. U. S. A.* 109:E2433-40. doi:10.1073/pnas.1207811109.
636 Greenberg, M.J., and E.M. Ostap. 2013. Regulation and control of myosin-I by the motor and
637 light chain-binding domains. *Trends Cell Biol.* 23:81–9. doi:10.1016/j.tcb.2012.10.008.
638 Greenberg, M.J., H. Shuman, and E.M. Ostap. 2017. Measuring the Kinetic and Mechanical
639 Properties of Non-processive Myosins Using Optical Tweezers. *Methods Mol. Biol.*
640 1486:483–509. doi:10.1201/b22505.
641 Grosshans, B.L., H. Grötsch, D. Mukhopadhyay, I.M. Fernández, J. Pfannstiel, F.-Z. Idrissi, J.

642 Lechner, H. Riezman, and M.I. Geli. 2006. TEDS site phosphorylation of the yeast
643 myosins I is required for ligand-induced but not for constitutive endocytosis of the G
644 protein-coupled receptor Ste2p. *J. Biol. Chem.* 281:11104–14.
645 doi:10.1074/jbc.M508933200.
646 Hassinger, J.E., G. Oster, D.G. Drubin, and P. Rangamani. 2017. Design principles for robust
647 vesiculation in clathrin-mediated endocytosis. *Proc. Natl. Acad. Sci. U. S. A.* 114:E1118–
648 E1127. doi:10.1073/pnas.1617705114.
649 Idrissi, F.-Z., A. Blasco, A. Espinal, and M.I. Geli. 2012. Ultrastructural dynamics of proteins
650 involved in endocytic budding. *Proc. Natl. Acad. Sci. U. S. A.* 109:E2587–E2594.
651 doi:10.1073/pnas.1202789109.
652 Idrissi, F.Z., H. Grötsch, I.M. Fernández-Golbano, C. Presciatto-Baschong, H. Riezman, and
653 M.I. Geli. 2008. Distinct acto/myosin-I structures associate with endocytic profiles at
654 the plasma membrane. *J. Cell Biol.* 180:1219–1232. doi:10.1083/jcb.200708060.
655 Joensuu, M., I. Belevich, O. Rämö, I. Nevzorov, H. Vihinen, M. Puhka, T.M. Witkos, M. Lowe,
656 M.K. Vartiainen, and E. Jokitalo. 2014. ER sheet persistence is coupled to myosin 1c-
657 regulated dynamic actin filament arrays. *Mol. Biol. Cell*. 25:1111–1126.
658 doi:10.1091/mbc.E13-12-0712.
659 Jonsdottir, G. a., and R. Li. 2004. Dynamics of Yeast Myosin I: Evidence for a Possible Role in
660 Scission of Endocytic Vesicles. *Development*. 14:1604–1609. doi:10.1016/j.
661 Jontes, J.D., E.M. Wilson-Kubalek, and R.A. Milligan. 1995. A 32 degree tail swing in brush
662 border myosin I on ADP release. *Nature*. 378:751–753. doi:10.1038/378751a0.
663 Kaksonen, M., Y. Sun, and D.G. Drubin. 2003. A pathway for association of receptors,
664 adaptors, and actin during endocytic internalization. *Cell*. 115:475–87.

665 Kaksonen, M., C.P. Toret, and D.G. Drubin. 2005. A modular design for the clathrin- and
666 actin-mediated endocytosis machinery. *Cell*. 123:305–20.
667 doi:10.1016/j.cell.2005.09.024.
668 Kaplan, C., S.J. Kenny, X. Chen, J. Schöneberg, E. Sitarska, A. Diz-Muñoz, M. Akamatsu, K. Xu,
669 and D.G. Drubin. 2022. Load adaptation by endocytic actin networks. *Mol. Biol. Cell*. 33.
670 doi:10.1091/mbc.E21-11-0589.
671 Krendel, M., E.K. Osterweil, and M.S. Mooseker. 2007. Myosin 1E interacts with
672 synaptojanin-1 and dynamin and is involved in endocytosis. *FEBS Lett.* 581:644–50.
673 doi:10.1016/j.febslet.2007.01.021.
674 De La Cruz, E.M., and E.M. Ostap. 2009. Kinetic and Equilibrium Analysis of the Myosin
675 ATPase. *Methods Enzymol.* 455:157–192. doi:10.1016/S0076-6879(08)04206-7.
676 Laakso, J.M., J.H. Lewis, H. Shuman, and E.M. Ostap. 2008. Myosin I can act as a molecular
677 force sensor. *Science*. 321:133–6. doi:10.1126/science.1159419.
678 Laakso, J.M., J.H. Lewis, H. Shuman, and E.M. Ostap. 2010. Control of myosin-I force sensing
679 by alternative splicing. *Proc. Natl. Acad. Sci. U. S. A.* 107:698–702.
680 doi:10.1073/pnas.0911426107.
681 Lewellyn, E.B., R.T. Pedersen, J. Hong, R. Lu, H.M. Morrison, and D.G. Drubin. 2015. An
682 Engineered Minimal WASP-Myosin Fusion Protein Reveals Essential Functions for
683 Endocytosis. *Dev. Cell*. 35:281–294. doi:10.1016/j.devcel.2015.10.007.
684 Lewis, J.H., T. Lin, D.E. Hokanson, and E.M. Ostap. 2006. Temperature dependence of
685 nucleotide association and kinetic characterization of Myo1b. *Biochemistry*. 45:11589–
686 97. doi:10.1021/bi0611917.
687 Lin, T., N. Tang, and E.M. Ostap. 2005. Biochemical and motile properties of Myo1b splice

688 isoforms. *J. Biol. Chem.* 280:41562–41567. doi:10.1074/jbc.M508653200.
689 Manenschijn, H.E., A. Picco, M. Mund, J. Ries, and M. Kaksonen. 2019. Type-I myosins
690 promote actin polymerization to drive membrane bending in endocytosis. *Elife*.
691 17:490011. doi:10.1101/490011.
692 El Mezgueldi, M., N. Tang, S.S. Rosenfeld, and E.M. Ostap. 2002. The Kinetic Mechanism of
693 Myo1e (Human Myosin-IC ). *J. Biol. Chem.* 277. doi:10.1074/jbc.M200713200.
694 Mogilner, A., and G. Oster. 1996. Cell motility driven by actin polymerization. *Biophys. J.*
695 71:3030–3045. doi:10.1016/S0006-3495(96)79496-1.
696 Mogilner, A., and G. Oster. 2003. Force Generation by Actin Polymerization II: The Elastic
697 Ratchet and Tethered Filaments. *Biophys. J.* 84:1591–1605. doi:10.1016/S0006-
698 3495(03)74969-8.
699 Mund, M., J.A. Van Der Beek, J. Deschamps, S. Dmitrieff, P. Hoess, J.L. Monster, A. Picco, F.
700 Nedelec, M. Kaksonen, and J. Ries. 2018. Systematic Nanoscale Analysis of Endocytosis
701 Links Efficient Vesicle Formation to Patterned Actin Nucleation. *Cell*. 174:884–896.
702 doi:10.1016/j.cell.2018.06.032.
703 Nickaeen, M., J. Berro, T.D. Pollard, and B.M. Slepchenko. 2019. Actin assembly produces
704 sufficient forces for endocytosis in yeast. *Mol. Biol. Cell*. 30:2014–2024.
705 doi:10.1091/mbc.E19-01-0059.
706 Pedersen, R.T., and D.G. Drubin. 2019. Type I myosins anchor actin assembly to the plasma
707 membrane during clathrin-mediated endocytosis. *J. Cell Biol.* 218:1138–1147.
708 doi:10.1083/jcb.201810005.
709 Picco, A., M. Mund, J. Ries, F. Nedelec, and M. Kaksonen. 2015. Visualizing the functional
710 architecture of the endocytic machinery. *Elife*. 4:1–29. doi:10.7554/eLife.04535.

711 Pyrpassopoulos, S., G. Arpağ, E.A. Feeser, H. Shuman, E. Tüzel, and E.M. Ostap. 2016. Force
712 generation by membrane-associated myosin-I. *Sci. Rep.* 6:1–14.
713 doi:10.1038/srep25524.
714 Roy, M.A., N. Siddiqui, and D. D'Amours. 2011. Dynamic and selective DNA-binding activity
715 of Smc5, a core component of the Smc5-Smc6 complex. *Cell Cycle*. 10:690–700.
716 doi:10.4161/cc.10.4.14860.
717 Skruzny, M., T. Brach, R. Ciuffa, S. Rybina, M. Wachsmuth, and M. Kaksonen. 2012.
718 Molecular basis for coupling the plasma membrane to the actin cytoskeleton during
719 clathrin-mediated endocytosis. *Proc. Natl. Acad. Sci. U. S. A.* 109:E2533–E2542.
720 doi:10.1073/pnas.1207011109.
721 Snoberger, A., B. Barua, J.L. Atherton, H. Shuman, E. Forgacs, Y.E. Goldman, D.A.
722 Winkelmann, and E.M. Ostap. 2021. Myosin with hypertrophic cardiac mutation r712l
723 has a decreased working stroke which is rescued by omecamtiv mecarbil. *Elife*. 10:1–
724 24. doi:10.7554/eLife.63691.
725 Sokac, A.M., C. Schietroma, C.B. Gundersen, and W.M. Bement. 2006. Myosin-1c couples
726 assembling actin to membranes to drive compensatory endocytosis. *Dev. Cell*. 11:629–
727 40. doi:10.1016/j.devcel.2006.09.002.
728 Spudich, J.A., and S. Watt. 1971. The Regulation of Rabbit Skeletal Muscle Contraction. *J.*
729 *Biol. Chem.* 246:4866–4871.
730 Stewart, T.J., V. Murthy, S.P. Dugan, and J.E. Baker. 2021. Velocity of myosin-based actin
731 sliding depends on attachment and detachment kinetics and reaches a maximum when
732 myosin-binding sites on actin saturate. *J. Biol. Chem.* 297.
733 doi:10.1016/j.jbc.2021.101178.

734 Sun, Y., A.C. Martin, and D.G. Drubin. 2006. Endocytic Internalization in Budding Yeast
735 Requires Coordinated Actin Nucleation and Myosin Motor Activity. *Dev. Cell*. 11:33–46.
736 doi:10.1016/j.devcel.2006.05.008.
737 Sun, Y., J. Schöneberg, X. Chen, T. Jiang, C. Kaplan, K. Xu, T.D. Pollard, and D.G. Drubin. 2019.
738 Direct comparison of clathrin-mediated endocytosis in budding and fission yeast
739 reveals conserved and evolvable features. *Elife*. 8. doi:10.7554/eLife.50749.
740 Takagi, Y., E.E. Homsher, Y.E. Goldman, and H. Shuman. 2006. Force generation in single
741 conventional actomyosin complexes under high dynamic load. *Biophys. J.* 90:1295–
742 1307. doi:10.1529/biophysj.105.068429.
743 Veigel, C., L.M. Coluccio, J.D. Jontes, J.C. Sparrow, R. a Milligan, and J.E. Molloy. 1999. The
744 motor protein myosin-I produces its working stroke in two steps. *Nature*. 398:530–
745 533. doi:10.1038/19104.
746 Woody, M.S., M.J. Greenberg, B. Barua, D.A. Winkelmann, Y.E. Goldman, and E.M. Ostap.
747 2018. Positive cardiac inotrope omecamtiv mecarbil activates muscle despite
748 suppressing the myosin working stroke. *Nat. Commun.* 9. doi:10.1038/s41467-018-
749 06193-2.
750 Woody, M.S., J.H. Lewis, M.J. Greenberg, Y.E. Goldman, and E.M. Ostap. 2016. MEMLET: An
751 Easy-to-Use Tool for Data Fitting and Model Comparison Using Maximum-Likelihood
752 Estimation. *Biophys. J.* 111:273–282. doi:10.1016/j.bpj.2016.06.019.
753 Woody, M.S., E.M. Ostap, Y.E. Goldman, and M. Capitanio. 2017. An ultra-fast EOD-based
754 force-clamp detects rapid biomechanical transitions. SPIE-Intl Soc Optical Eng. 26.
755

756 **Figure 1: Models for the functions of actin assembly and myosin activity during**
757 **membrane deformation for clathrin-mediated endocytosis**
758 Cartoon diagram illustrating the organization of actin filaments and Myo5 molecules at
759 endocytic sites. Actin filaments are bound by coat proteins at the tip of the growing
760 membrane invagination and oriented with their growing ends toward the plasma
761 membrane, powering membrane invagination. The type I myosin Myo5 could either anchor
762 the actin network in a favorable orientation (left) or provide an assisting force (right).
763
764 **Figure 2: In-solution, population biochemical characterization of Myo5**
765 **(A)** Coomassie-stained SDS-polyacrylamide gels showing example preparations of the
766 purified Myo5 motor/lever construct and calmodulin (Cmd1, light chain) used in all
767 experiments. **(B)** The actin concentration dependence of the steady-state ATPase activity of
768 100 nM unphosphorylated (grey circles) and phosphorylated Myo5 (black circles). Each
769 data point represents the average of 6-7 time courses, which were 100 s each. The orange
770 line is a best fit of the phosphorylated Myo5 data to a rectangular hyperbola. **(C)** Schematic
771 pathway for the Myo5 ATPase cycle. Blue motors are in tightly bound conformations, green
772 motors are weakly bound/unbound. **(D)** Example light scattering transients reporting on
773 ATP-induced dissociation of phosphorylated (left, $k_{obs}$ = 17 $s^{-1}$) and unphosphorylated
774 (right, $k_{obs}$ = 64.1 $s^{-1}$) actoMyo5, obtained by mixing 100 nM actoMyo5 (AM) with 94 μm
775 and 72 μM ATP, respectively, as shown in the inset schematic. The black line is the fit of a
776 single exponential function to the data. **(E)** ATP concentration dependence of dissociation
777 of 100 nM unphosphorylated (grey circles) and phosphorylated actoMyo5 (black circles).
778 Each data point represents 3-6 time courses averaged and fit to a single exponential decay

779 function. The orange line is a linear best fit of the phosphorylated Myo5 data. The purple
780 line is a best fit of the unphosphorylated Myo5 data to a rectangular hyperbola.
781 **(F)** Example light scattering transients reporting ATP-induced dissociation of ADP-
782 saturated phosphorylated (left) and unphosphorylated (right) actoMyo5, obtained by
783 preincubating 200 nM actoMyo5 (AM) with 100 μM ADP, then mixing rapidly with 2.5 mM
784 ATP, as shown in the inset schematic. The black line is the fit of a single exponential
785 function to the data. **(G)** Velocity of actin filament gliding, measured at varying surface
786 densities of Phospho-Myo5 (black circles, orange line) and unphosphorylated Myo5 (gray
787 circles, purple line) in in vitro motility assays. Myosin concentrations indicate the quantity
788 of protein incubated in the flow chamber before washing. Each data point represents the
789 average velocity of 30 – 60 filaments, and the error bars are standard deviations.
790
791 **Table 1**
792 Summary of rate and equilibrium constants measured for Myo5 in this study. Errors are
793 standard errors of the fits.
794
795 **Figure 3: Single molecule, optical trap analysis of Myo5 step size and kinetics**
796 **(A)** Cartoon schematic of the 3-bead optical trapping setup. A biotinylated actin filament is
797 tethered between two neutravidin-coated beads that are trapped in a dual beam optical
798 trap. This bead-actin-bead "dumbbell" is lowered onto pedestal beads that have been
799 sparsely coated with $His_6$ antibody to attach Myo5-motor/lever-Avi-Tev-$His_9$. **(B-D)** Single
800 Myo5 displacements of a single bead position and covariance traces, calculated using both
801 beads, showing single molecule interactions acquired in the presence of 1 μM **(B)** 10 μM

802 **(C)** and 1000 μM ATP. **(D)**. Blue bars indicate attachment events as identified by covariance
803 (gray) decreases. The threshold of event detection by the covariance traces are indicated
804 by dashed gray lines. **(E)** Schematic of displacement traces depicting the 2-step nature of
805 actomyosin displacements in the optical trap. **(F-H)** Binding events were synchronized at
806 their beginnings (left) or ends (right) and averaged forward or backward in time,
807 respectively. Measured total displacement of Myo5 was 5.0 nm at 10 μM ATP, with the 1$^{st}$
808 substep contributing a 4.8 nm displacement (arrow 1. in G) and the 2$^{nd}$ substep
809 contributing a 0.2 nm displacement (arrow 2. In G). **(F-H, left)** Forward-averaged
810 ensembles synchronized at the beginnings of events. **(F-H, right)** Reverse-averaged
811 ensembles synchronized at the ends of events. Black and gray lines are single exponential
812 fits in the forward and reverse ensembles, respectively. **(I)** Cumulative distributions of
813 attachment durations for Myo5 at 1, 10, and 1000 μM ATP. Blue lines show cumulative
814 frequency of attachment durations at the indicated ATP concentrations, and the red,
815 yellow, and green lines indicate fitted exponential distributions at 1, 10, and 1000 μM ATP,
816 respectively. 1 and 10 μM ATP were fit well to single exponentials, and the 1000 μM ATP
817 data were best described by the sum of two exponentials. **(J)** Summary of rates at 1, 10, and
818 1000 μM ATP calculated from (F-H). Blue boxes are the fitted exponential distributions
819 from (I), black diamonds are forward ensemble fits from (F-H, left), and gray diamonds are
820 reverse ensemble fits from (F-H, right). At lower concentrations of ATP (1 and 10 μM), the
821 rate of detachment is limited by ATP association, corresponding to the reverse ensemble
822 fits, while at saturating ATP concentration (1000 μM), the detachment rate is limited by the
823 rate of ADP dissociation, corresponding to the forward ensemble fits. **(K)** Summary of rates
824 determined via single molecule optical trapping. Errors for detachment rates are 95%

825 confidence intervals. Errors for forward and reverse ensemble fits are standard errors of
826 the fits. *Detachment rates at 1000 μM ATP were best fit to the sum of 2 exponents. The
827 major component of the fit (67.8 $s^{-1}$) comprises 92.1% of the total with the remaining 7.9%
828 having a rate of 11.6 $s^{-1}$.
829
830 **Figure 4: Myo5 attachment lifetimes are substantially less force-dependent than**
831 **other known type I myosins**
832 An isometric optical force clamp was utilized to determine the force-sensitivity of the
833 detachment of Myo5 from actin. **(A)** Durations of individual actomyosin attachments as a
834 function of force, plotted on a semi-log scale **(B)** The solid black line shows the force
835 dependence of the detachment rates determined by MLE fitting of unaveraged points in A.
836 For illustration purposes, attachment durations from (A) were binned by force at every 10
837 points, averaged, and converted to rates. Best- fit parameters were determined by MLE
838 fitting and 95% confidence intervals were calculated via bootstrapping. The solid black line
839 is calculated from best fit parameters (k = 67.6 $s^{-1}$, d = 1.14 nm), while the gray shaded
840 region is the 95% confidence interval (k = 62.4-72.9 $s^{-1}$, d = 1.03-1.26 nm). All MLE fitting
841 was performed on unaveraged data and was corrected for instrument deadtime. **(C)** The
842 force dependent detachment rate of Myo5 (from panel B) plotted alongside the force
843 dependent detachment rates for Myo1b, Myo1c, and β-cardiac muscle myosin, Myh7. **(D)**
844 Power output for the same four myosins calculated over a range of forces by multiplying
845 the functions from (C) by the applied force F, and the step size and duty ratios of each
846 myosin.
847

848 **Figure S1: P21 Activated Kinase 1 (Pak1) phosphorylates Myo5 on S357**

849 Crude preparations of wild type and S357A Myo5 motor/lever constructs were mixed with
850 250 μM ATP including 20 μCi of ATPγP32 in kinase assay buffer (5 mM MOPS pH 7, 2.5 mM
851 β-glycerophosphate, 5 mM $MgCl_2$, 400 μM EDTA, 1 mM EGTA, 50 μM DTT) in either the
852 presence or absence of Pak1. Reactions were incubated at 25˚C for 60 minutes, then
853 quenched by adding an equal volume of 2x tris urea sample buffer (125 mM Tris pH 6.8,
854 6 M urea, 2% SDS, 0.1% bromophenol blue, 10% β-mercaptoethanol) and resolved on a
855 10% polyacrylamide gel. The gel was stained with Coomassie, then dried onto Whatman
856 paper and exposed to a storage phosphor screen (Amersham). The Coomassie-stained gel
857 was imaged on a standard photo scanner and the phosphor screen on a Typhoon gel imager
858 (Amersham). Note that there are differences in baseline labeling in the absence of added
859 kinase between the two different protein preps, but addition of Pak1 clearly results in
860 radiolabeling of wild type but not mutant Myo5.

861

862 **Movie S1: Motility assays with phosphorylated Myo5**

863 Rhodamine phalloidin-labeled actin filaments gliding over coverslips coated with a
864 concentration series of phosphorylated Myo5 protein in motility buffer with 1 mM ATP.
865 Movies were collected at 1 frame per second and are played back at 16 frames per second.

866

867

868 **Movie S2: Motility assays with unphosphorylated Myo5**

869 Rhodamine phalloidin-labeled actin filaments gliding over coverslips coated with a
870 concentration series of unphosphorylated Myo5 protein in motility buffer with 1 mM ATP.

871 Short movies of motility at 100 nM and 150 nM unphosphorylated Myo5 were collected
872 because no motility was observed. Movies at all other concentrations were collected at 1
873 frame every 4 seconds and are played back at 16 frames per second. The playback rate of
874 Movie S2 is four times faster than the playback rate of Movie S1.

**Figure 1**

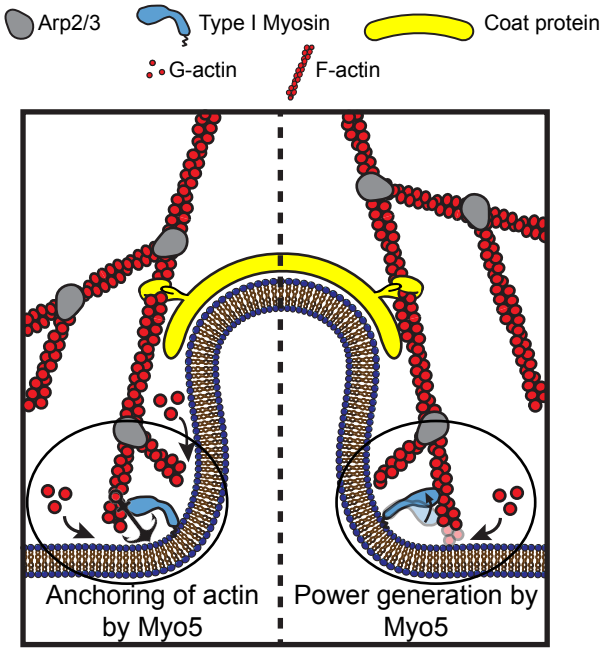
Arp2/3
Type I Myosin
Coat protein
G-actin
F-actin
Anchoring of actin by Myo5
Power generation by Myo5

**Table 1: Rate and equilibrium constants of the Myo5 ATPase cycle**

| | Phosphorylated Myo5 | Unphosphorylated Myo5 |
|---|---|---|
| **Steady-state actin-activated ATPase** | | |
| $V_{max}$ ($s^{-1}$) | 3.3 (± 0.15) | ND |
| $K_{ATPase}$ (μM) | 5.1 (± 0.88) | ND |
| **ATP binding** | | |
| $K_1'$ ($\mu M^{-1}$) | ND | 0.006 (± 0.0016) |
| $k_{+2}'$ ($s^{-1}$) | ≥ 335 | 290 (± 24) |
| $K_1'k_{+2}'$ ($\mu M^{-1}$ $s^{-1}$)[a] | 0.39 (± 0.017)[b] | 1.1 (± 0.28)[c] |
| **ADP release** | | |
| $k_{+5}'$ ($s^{-1}$) | 74 (± 2.0) | 107 (± 5.9) |

[a]Determined from a linear fit of the unbinding rates. [b]Linear fit of all data for Phosphorylated Myo5 in Fig. 2E. [c]Linear fit of observed rates below 100 μM ATP for Unphosphorylated Myo5 in Fig 2E. ND: Not Determined.

# Figure 2

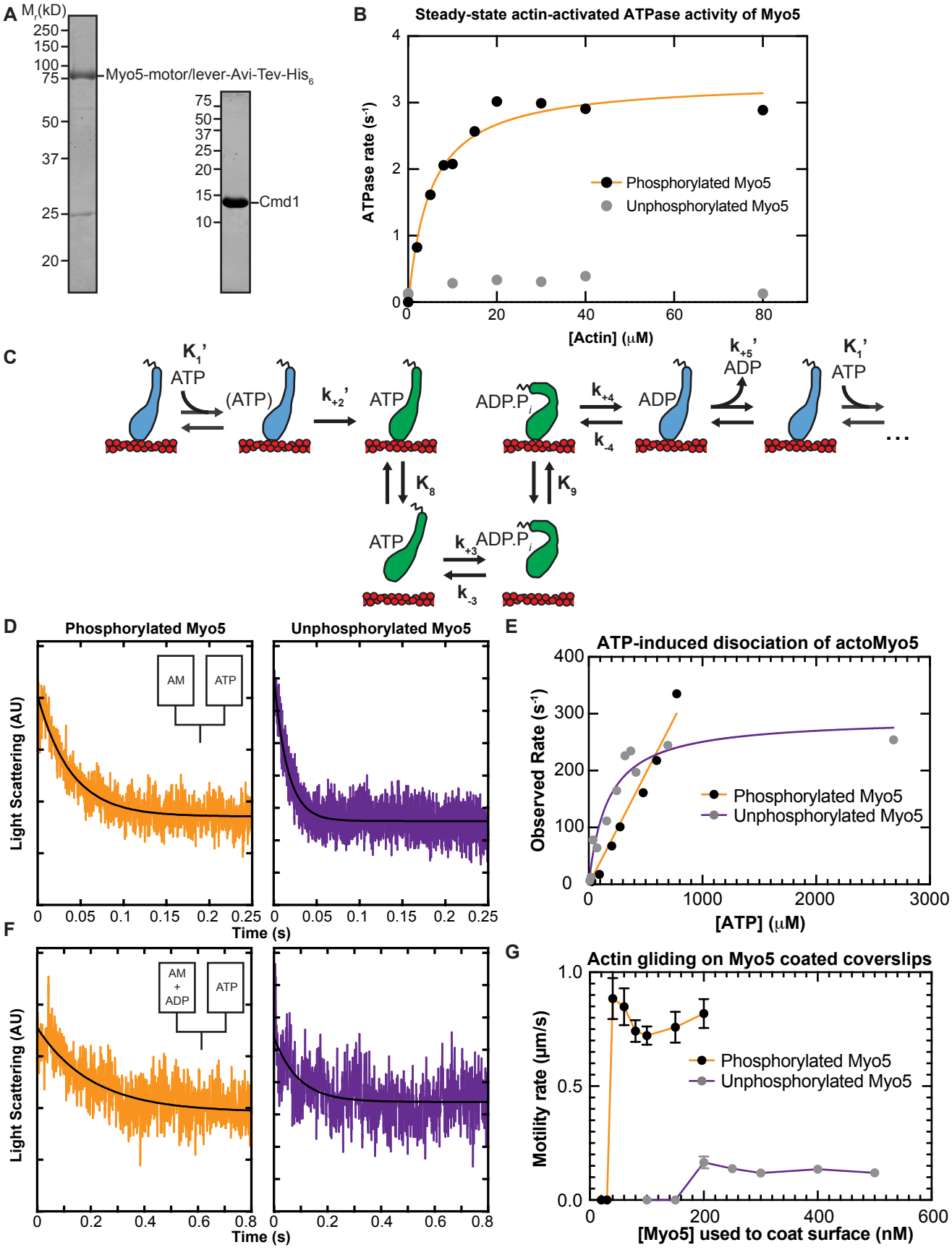
A
Mr(kD)
250
150
100
75
50
37
25
20
Myo5-motor/lever-Avi-Tev-His6
75
50
37
25
20
15
10
Cmd1
B
Steady-state actin-activated ATPase activity of Myo5
ATPase rate (s-1)
[Actin] (μM)
Phosphorylated Myo5
Unphosphorylated Myo5
C
K1'
ATP
(ATP)
k+2'
ATP
ADP.Pi
k+4
k-4
ADP
k+5'
ADP
K1'
ATP
K8
K9
ATP
k+3
ADP.Pi
k-3
D
Phosphorylated Myo5
Unphosphorylated Myo5
AM
ATP
Light Scattering (AU)
Time (s)
E
ATP-induced disociation of actoMyo5
Observed Rate (s-1)
[ATP] (μM)
Phosphorylated Myo5
Unphosphorylated Myo5
F
AM + ADP
ATP
Light Scattering (AU)
Time (s)
G
Actin gliding on Myo5 coated coverslips
Motility rate (μm/s)
[Myo5] used to coat surface (nM)
Phosphorylated Myo5
Unphosphorylated Myo5

## Figure 3

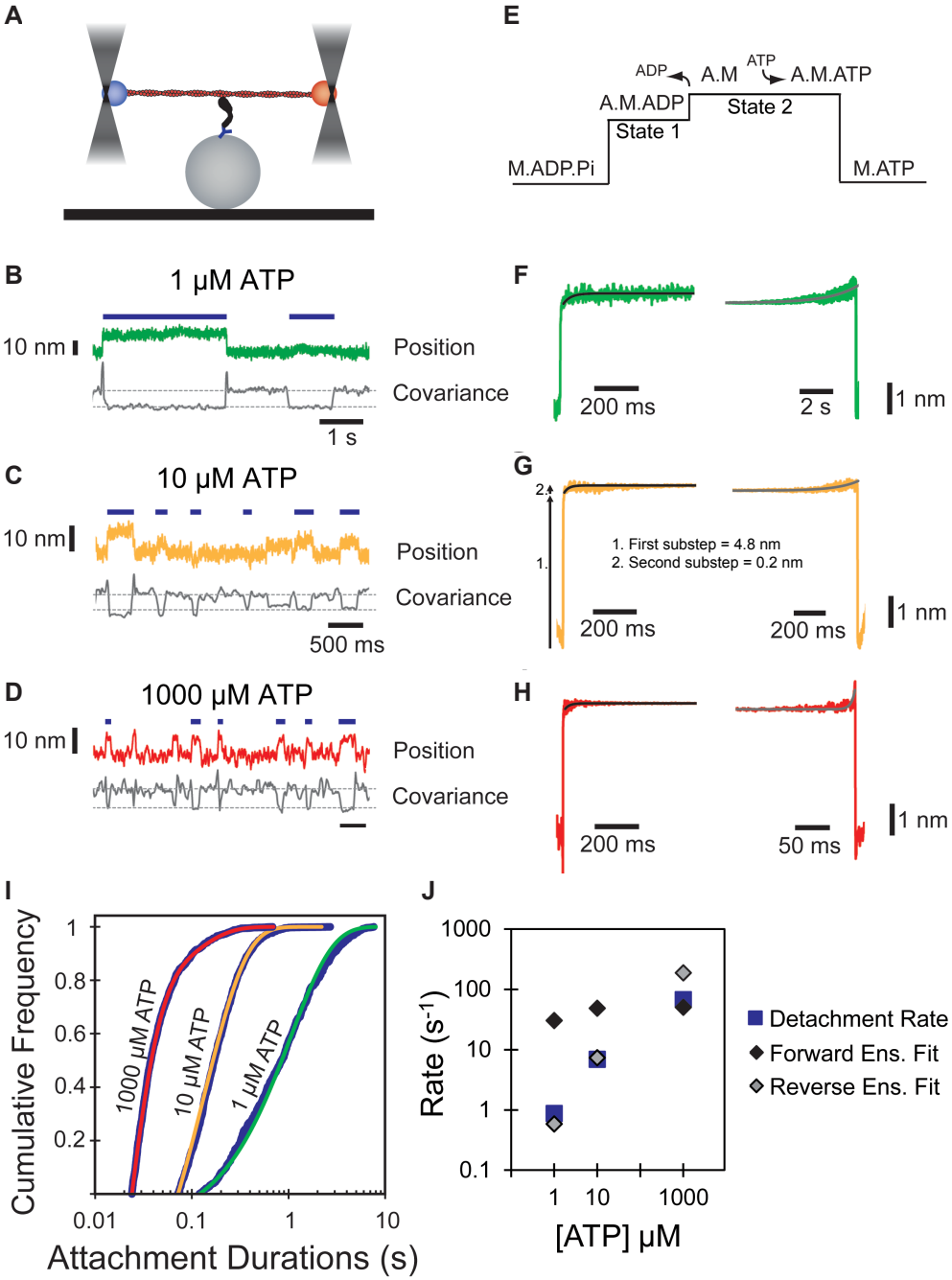


K

**Summary of rates determined during single molecule optial trapping**

| [ATP] μM | Detachment Rate ($s^{-1}$) | Forward Ensemble Fit ($s^{-1}$) | Reverse Ensemble Fit ($s^{-1}$) |
|---|---|---|---|
| 1 | 0.88 (+/- 0.07/0.07) | >30 | 0.59 (+/- 0.003) |
| 10 | 6.9 (+/- 0.49/0.46) | 49 (+/- 1.6) | 7.3 (+/- 0.1) |
| 1000 | 67.8* (+/- 11.9/8.7) | 50 (+/- 0.2) | >187 |

**Figure 4**

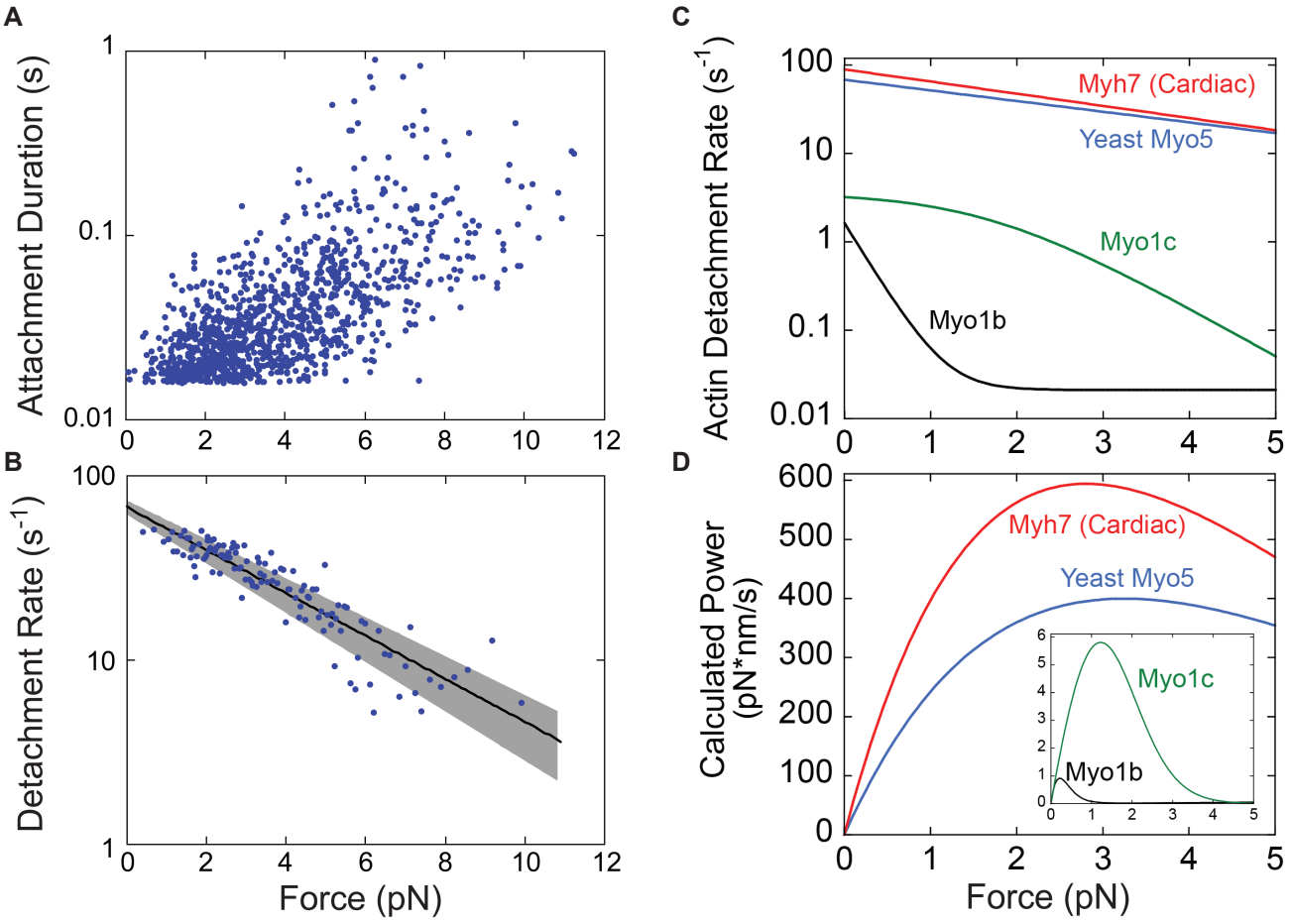
A
Attachment Duration (s)
1
0.1
0.01
0
2
4
6
8
10
12
B
Detachment Rate (s-1)
100
10
1
Force (pN)
C
Actin Detachment Rate (s-1)
100
10
1
0.1
0.01
Myh7 (Cardiac)
Yeast Myo5
Myo1c
Myo1b
0
1
2
3
4
5
D
Calculated Power (pN*nm/s)
600
500
400
300
200
100
0
Myh7 (Cardiac)
Yeast Myo5
Myo1c
Myo1b
Force (pN)